Nanorobots Sense Local Physicochemical Heterogeneities of Tumor Matrisome

Debayan Dasgupta[1,#], Dharma Pally[2,#], Deepak K. Saini[2,3], Ramray Bhat[2,*] and Ambarish Ghosh[1,4,*]

[1] Centre for Nano Science and Engineering, Indian Institute of Science, Bangalore 560012, India

[2] Department of Molecular Reproduction, Development and Genetics, Indian Institute of Science, Bangalore 560012, India

[3] Centre for Biosystems Science and Engineering, IISc, Bangalore 560012, India

[4] Department of Physics, Indian Institute of Science, Bangalore 560012, India

[#]Equal contributing authors

*Corresponding authors

Keywords: *Nanorobots, cancer microenvironment, extracellular matrix, tumorigenesis, adhesion, sialic acid*

Abstract:

The dissemination of cancer is brought about by continuous interaction of malignant cells with their surrounding tissue microenvironment. Understanding and quantifying the remodeling of local extracellular matrix (ECM) by invading cells can therefore provide fundamental insights into the dynamics of cancer dissemination. In this paper, we use an active and untethered nanomechanical tool, realized as magnetically driven nanorobots, to locally probe a 3D tissue culture microenvironment consisting of cancerous and non-cancerous epithelia, embedded within reconstituted basement membrane (rBM) matrix. Our assay is designed to mimic the *in vivo* histopathological milieu of a malignant breast tumor. We find that nanorobots preferentially adhere to the ECM near cancer cells: this is due to the distinct charge conditions of the cancer-remodeled ECM. Surprisingly, quantitative measurements estimate that the adhesive force increases with the metastatic ability of cancer cell lines, while the spatial extent of the remodeled ECM was measured to be approximately 40 μm for all cancer cell lines studied here. We hypothesized and experimentally confirmed that specific sialic acid linkages specific to cancer-secreted ECM may be a major contributing factor in determining this adhesive behavior. The findings reported here can lead to promising applications in cancer diagnosis, quantification of cancer aggression, *in vivo* drug delivery applications, and establishes the tremendous potential of magnetic nanorobots for fundamental studies of cancer biomechanics.

Introduction:

Epithelial cancer cells invade from their primary site of tumorigenesis *in vivo* by remodeling their surrounding stromal extracellular matrix (ECM)[1,2]. A strong interdependency exists between the ECM and cancer cells: mechanical properties of the ECM dysregulates signaling within cancerous cells, resulting in aberrant expression of matrix and matricellular proteins, which in turn can alter the chemical and physical composition of the ECM. This reciprocal interplay has a profound effect on the progression of cancer[3,4]. Therefore, a quantitative understanding of the physical changes of cancer-sculpted ECM is of great importance in biophysical studies of tumorigenesis and

metastasis. This is not trivial, considering the physico-chemical composition of the cancer microenvironment is extremely heterogenous, arising due to three-dimensional localization of the fibrillar network of biopolymers like collagen, along with various non-fibrillar matrix proteins, proteoglycans, secreted factors and enzymes. As an alternative to traditional studies conducted on planar (two dimensional (2D)) cell cultures, current investigations have moved on to cells within three dimensional (3D) matrices, which mimic many of the physicochemical and mechanical properties of tumors *in vivo*[5–7 8]. Assays based on 3D matrix present a higher degree of complexity since the ECM stiffness, limited porosity and extensive polymer crosslinking observed in such environments typify the matrix microenvironment of *in vivo* tumors. Therefore 3D matrix can provide a model platform for biophysical investigations as well as test emergent cancer therapeutic strategies[9,10].

Apart from various imaging techniques, such as scanning electron microscopy of scaffolds used for tissue engineering[11], optical coherence tomography (OCT) using gold nanorods[12,13], time-lapse confocal reflection microscopy (TL-CRM)[14] and multiphoton imaging techniques[15], an experimental investigation of the local heterogeneities of 3D ECM environments has only been attempted with mechanical probes such as atomic force microscopy (AFM)[16,17] or particle tracking microrheology (PTM)[18,19]. While AFM studies are limited to probing the exposed surfaces of 3D matrices, the latter can measure the rheological parameters or trace out local mechanical anisotropies in the bulk matrix. However, measurements with untethered probes, such as used in PTM, are limited to a spatial range given by $\sqrt{Dt_e}$, where D and t_e refer to the diffusivity of the probe and duration of experiment respectively. Also, the probe positions are randomized due to thermal fluctuations, which prohibits making measurements at observer-specified locations.

Herein lies a major motivation of our study: can we drive the probes actively to measure the local heterogeneities of the ECM in well-defined and specifically chosen locations at high speeds? As we show here, this can be realized with remotely controlled motile nanoprobes moving in an ECM containing diverse epithelia, wherein the active probe can sense, map and even quantify cancer-induced heterogeneities within the ECM.

Our experimental approach was to use magnetically driven nanorobots as active probes and study their maneuverability in different regions of the recreated breast tumor microenvironment. The latter consisted of invasive as well as non-invasive breast cancer cells and immortalized non-transformed breast epithelia embedded within laminin-rich reconstituted basement membrane (rBM) matrix. The choice of rBM is guided by observations that the ECM that surrounds breast cells and is the first to be remodeled and degraded before the migration of cancer cells into the stroma, consists of non-fibrillar basement membrane proteins, including, but not limited to laminin[20–22]. Moreover, non-transformed and malignant breast epithelia when embedded in rBM form breast acini-like and invasive breast carcinoma-like cellular architectures[23–25].

The experimental platform comprises of helical nanostructures containing ferromagnetic elements which are subjected to rotating magnetic fields, where the chiral shape causes the rotating nanostructures to move forward or backward, depending on the handedness of the helix and sense of rotation of the field. This method[26–29] of remote manipulation of untethered nanorobots is shown to be more efficient[30] than conventional magnetic gradient pulling methods at small scales (also see SI: Section S1 and Figure S1). They also provide a promising route toward futuristic drug delivery vehicles[31–35], studies of cellular biophysics[36] as well as microfluidic manipulation[37–40], sensing applications[36,41] and selective sorting of cancer cells[42,43]. Indeed, these and similar other active nanostructures have been maneuvered in complex biological environments in the past[35,40]

[44]; however, we must stress that our findings are fundamentally different from all previous experiments. While the primary motivation in the past was to demonstrate maneuverability of the nanorobots in a certain biological environment, here, we use variations of maneuverability as a tool to quantify the changes in physical properties of the ECM that is proximal to, and sculpted by, cancer cells. The difference in such properties between cancer cells and surrounding normal cells contributes to the heterogeneity of tumor microenvironment.

Results:

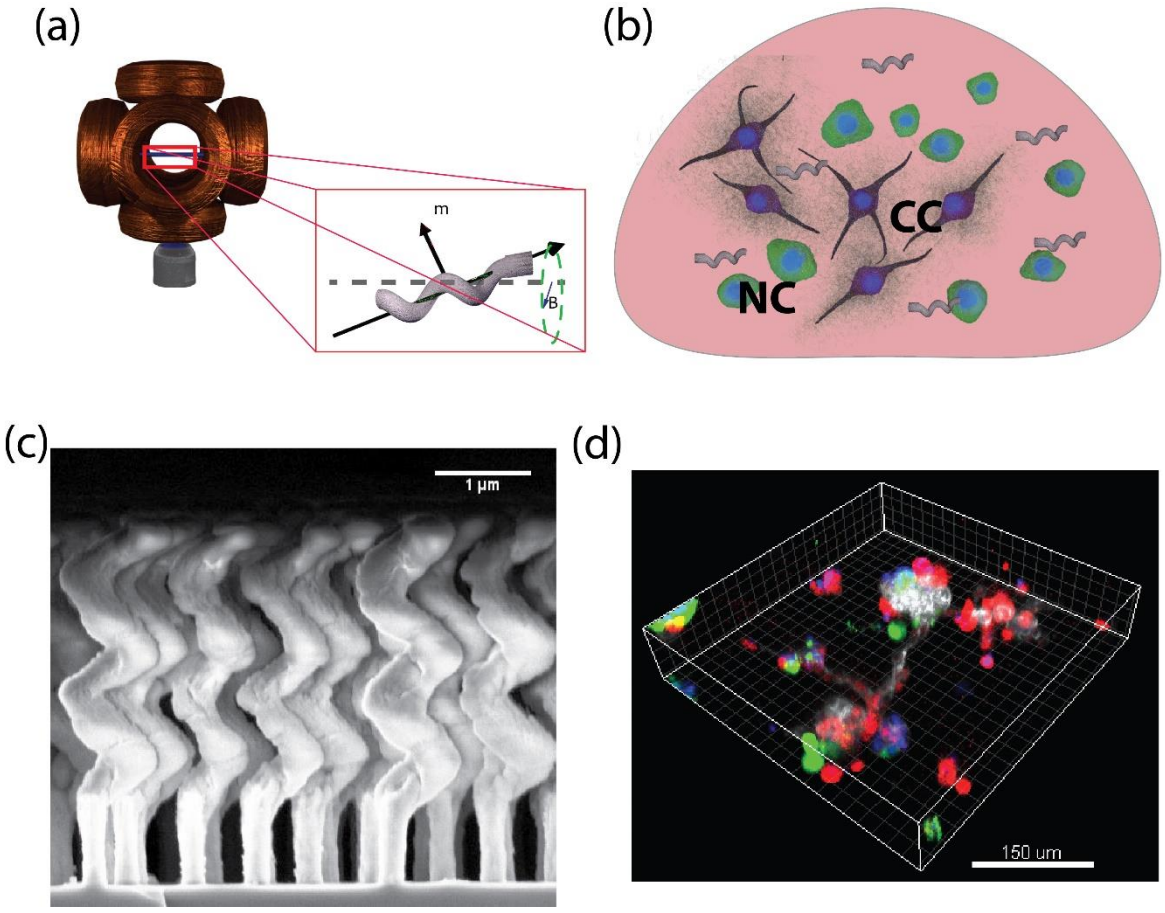

Figure 1: Experimental setup

(a) Schematic representation of the experimental setup where the heterogenous 3D culture is placed within a triaxial Helmholtz coil built around a fluorescence microscope; the inset shows a schematic depiction of a nanorobot with magnetic material embedded inside its helix. The magnetic moment vector is represented by the vector 'm' which is subjected to an externally applied rotating magnetic field 'B'. (b) Schematic depiction of a 3D co-culture containing cancer cells (labelled as CC, purple), non-transformed cells (labelled NC, green) and helical nanorobots. (c) Scanning electron microscope image of nanorobots grown on silicon pillars by Glancing Angle Deposition (d) Confocal z-stack reconstruction of a 3D reconstituted Basement Membrane (rBM) scaffold with cells: invasive breast cancer cells with constitutive expression of red fluorescent protein (RFP MDA-MB-231) and the non-transformed cells with constitutive expression of green fluorescent protein (GFP HMLE). DNA within nuclei is shown in blue after staining with DAPI (all the colors are overlaid to generate the shown image).

Magnetically guided nanorobots of 250 nm width maneuver through reconstituted basement-membrane (rBM) matrix

The motion of nanorobots in biologically complex environments depend on several factors. Corrosion from surrounding medium can result in loss of magnetic property and therefore motility, which necessitates the use of protective layers[34] around the magnetic material. For media containing suspended cells such as blood, the motility can be limited by colloidal jamming of the blood cells, resulting in stick and slip type of motion[34]. In more solid-like media, e.g. ECM, the porous fibrous network of biopolymers can provide strong hindrance[45]. To achieve motility, the width of the helical shape therefore needs to be less than the polymer porosity. This effect has been observed while moving helical nanorobots in gels and achieving controlled motility within living cells, where the filament width of the helices were 70 nm[40] and 250 nm[36] respectively. For the experiments described here, we checked the maneuverability within polymerized acellular laminin-rich reconstituted basement membrane matrix (lrBM). rBM mimics the ECM that breast cancer epithelia interact with, degrade and replace with freshly synthesized collagenous ECM during invasion[46] . We found helices of filament width 250 nm had significantly higher motility compared to helices of filament width 500 nm (see SI: Figure S2 to see electron microscope images of the helices), which is in general agreement[47,48] with previous measurements of porosity of polymerized rBM[49]. Further investigation with passive microrheological techniques in rBM using beads of diameter 200 nm indeed indicates existence of finer spatial structuring of sub-micron dimensions (see SI: Figure S3 and Section S3 for further details). We believe that the nanorobots with a filament width of 250 nm can easily move through the sub-micron pores in the rBM, however nanorobots with thicker filament width encounters increased resistance.

The maneuverability of thinner nanorobots implicitly proves the absence of, or significant reduction in, adhesive forces between the nanorobots and rBM in comparison to the propulsive thrust generated by the magnetic drive. Past research shows that strong adhesion with charged polymers adversely affects the motility of nanorobots, which could be overcome through enzymatic activity[50] or appropriate hydrophobic coatings[35]. In the present experiment, we investigated how the adhesive forces between the nanorobots and ECM get modified in a cancer microenvironment.

The experimental setup involves a triaxial Helmholtz coil as shown in Figure 1(a), which produces a rotating magnetic field. The nanorobots with ferromagnetic material embedded in the helix can follow the field generated by the Helmholtz coil thereby executing motion in the direction perpendicular to the plane of rotation (see Figure 1(a) inset). The microenvironmental co-culture was constituted as a 3D matrix scaffold of rBM, within which metastatic breast cancer cells MDA-MB-231 (labelled as CC and expressing Red Fluorescent Protein (RFP)) and non-cancerous breast epithelia HMLE (labeled as NC and expressing Green Fluorescent Protein (GFP)) were cultured (see schematic in Figure 1(b)). The helical structures (see Figure 1(c)) are fabricated by Glancing Angle Deposition[26] and injected into a cell-matrix co-culture which was placed inside the Helmholtz coil and observed through a fluorescence microscope. The complexity of the terrain traversed by the nanorobot could be gauged from the 3D reconstruction of z-stack images of the co-culture with RFP MDA-MB-231 and GFP HMLE (see Figure 1(d) and supplementary movie M1).

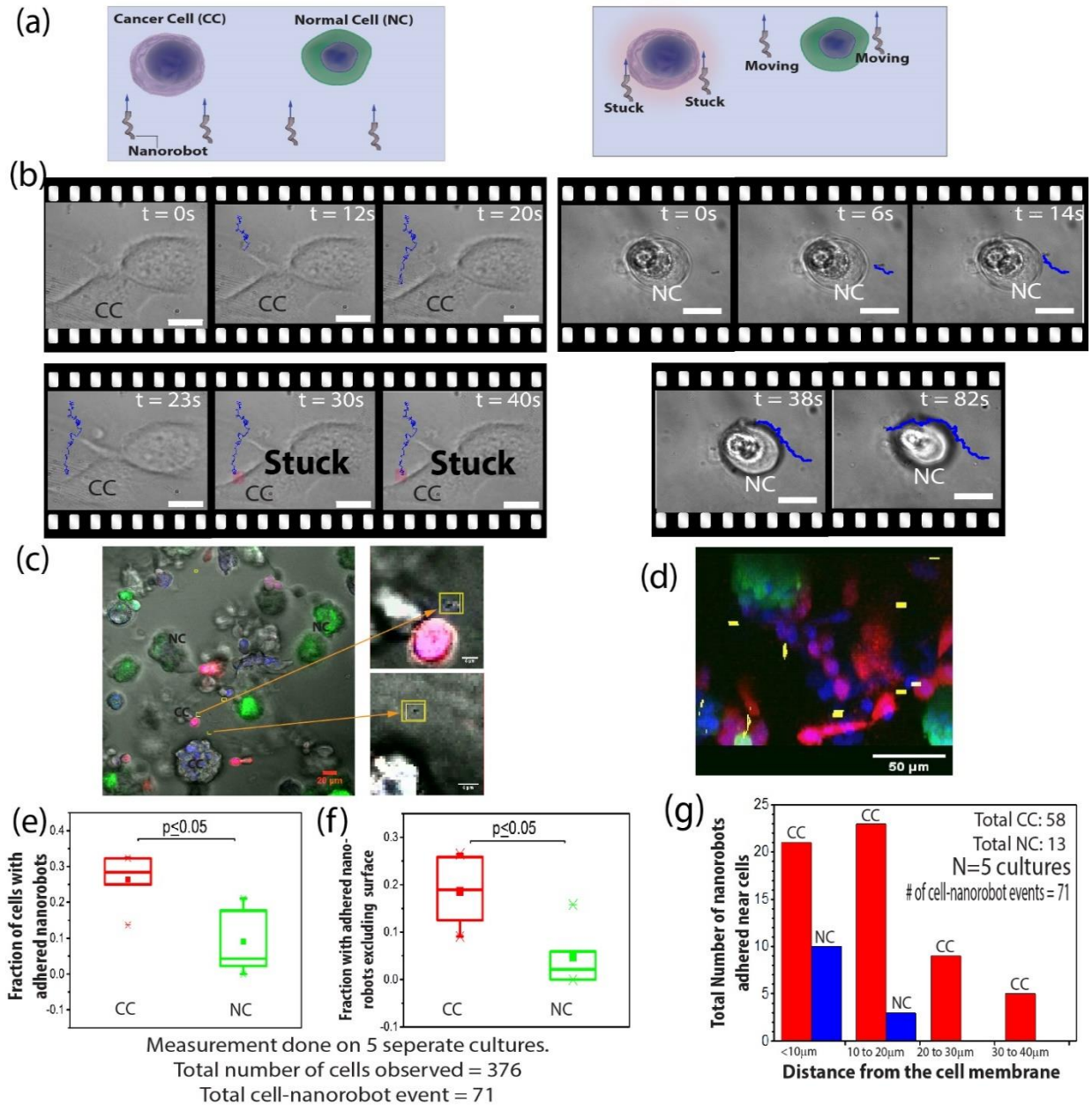

Figure 2: Analyzing the differential adhesion near cancerous cells (CC) and non-transformed breast cells (NC)

(a): Schematic representation of the experimental procedure wherein nanorobots are magnetically maneuvered within the 3D co-culture. We find the nanorobots to be preferentially adhered to the ECM near the CC. (b) A nanorobot approaching CC gets adhered in the ECM close to the cell as shown in the left panel (Also see movie M2a). However, as shown in the right panel, a nanorobot starting from the vicinity of a NC can be maneuvered away without adhering (See movies M2b and M2c). All scale bars correspond to 10 µm (c) A single slice from a stack of confocal micrographs showing nanorobots in the vicinity of a CC embedded in 3D rBM scaffold; nanorobots (yellow squares) can be localized predominantly in the vicinity of CC (RFP MDA-MB-231). The NC are shown in green (GFP HMLE). Insets show a zoomed in view of the nanorobots near the cells. (d) A side-view of 72 slices of z-stack showing adhered nanorobots at various planes (See movie M3). Location of nanorobots are highlighted in yellow. The lateral dimensions for this z-stack is 175 µm × 175 µm. (e) Box and whisker plots

showing the number of adhered nanorobots per cell for both CC and NC. The comparison was done with t-test of proportions. Each bar represents the mean ± SD for N = 5 different biological experiments. A total of 376 cells were sampled, away from the point of nanorobot injection, of which 203 cells were cancer cells and 173 were non-cancerous cells. Total 71 cells were found to have nanorobots adhered to the ECM in their vicinity, of which 58 were cancer cells and 13 were non-cancerous cells. The y-axis represents the fraction of cells with adhered nanorobots in their vicinity. The lower and upper bounds of the boxes represent the 25- and 75- percentile range of the data. The line dividing the box plot represents the median value. The whiskers represent the 1- and 99- percentile range. The mean is represented by the solid square dots. (f) Graphical representation of the same values measured in (e) with the exclusion of cells, where nanorobots adhered directly to the surface of the cells. (g) Bar graph showing the total number of adhered nanorobots as a function of distance from the cell surface from NC and CC. Only cells with nanorobots adhered to their surrounding ECM were recorded for this graph.

Maneuvered nanorobots preferentially adhere to ECM in the vicinity of cancer cells

A collection of nanorobots were injected into the tumor-like environment and moved unidirectionally for 30 minutes under constant magnetic field strength and frequency (experimental procedure shown in Figure 2(a)). Typically, the nanorobots moved along a random direction for up to 1000 μm. For observing the motion of a single nanorobot approaching a cell, 3D cultures containing just CC or NC were used. The panel in Figure 2(b) shows that a nanorobot approaching CC got adhered to the ECM in its vicinity, whereas a nanorobot approaching a NC interacts with it without getting adhered to the NC-proximal ECM (see movies M2a, M2b, M2c). Similar experiments were performed on 3D co-cultures (containing both CC and NC), where, after moving the nanorobots, the ECM was fixed to prevent further changes through cell migration or secretion. We imaged the ECM along all three spatial axes using confocal microscopy and found the nanorobots to be predominantly located close to the CC (see Figure 2(c)). As shown in Figure 2(d), the nanorobots were distributed across various planes, suggesting an exhaustive exploration of the heterogeneity in 3D space (also see movie M3). It is to be noted that these locations were significantly away from the point of injection (> 500 μm), greater than what would be expected due to passive diffusion of the nanorobots in rBM (see SI: Section S4). We observed that there is

a significantly higher probability of finding the nanorobots near cancer cells due to their preferential adhesion to ECM near cancer cells, (see Figure 2(e)). This observation was true even when nanorobots adhered to surfaces of cells were excluded from the analysis (see Figure 2(f)).

We analyzed 4 stacks of confocal images with an area of 350 μm × 350 μm, thereby sampling a net area of about ~0.5 mm^2 (see SI: Figure S4) to locate the adhered nanorobots and the cell(s) nearest to it. The cell fluorescent signal allowed us to identify whether the nearest cell was non-transformed (green) or cancerous (red). Most of the nanorobots near cancer cells were adhered to the ECM to within 20 μm from cells although smaller numbers could be seen up to 40 μm (see Figure 2(g)). Of the total 13 nanorobots that adhered close to non-cancerous cells, 7 were found to be adhered to their surfaces and only 6 in the ECM.

We did not consider nanorobots that were more than 40 μm away from any cell, given that it was possible that these nanorobots were moving and had still not adhered when the sample was fixed. The 40 μm length scale was chosen because we had observed very few nanorobots showing any form of adhesion to their surroundings beyond this distance from the cell surface, when their motion was observed under a rotating magnetic field. We hypothesized that the preferential adhesion near cancer epithelia was because the latter are known to remodel ECM in their vicinity[51,52].

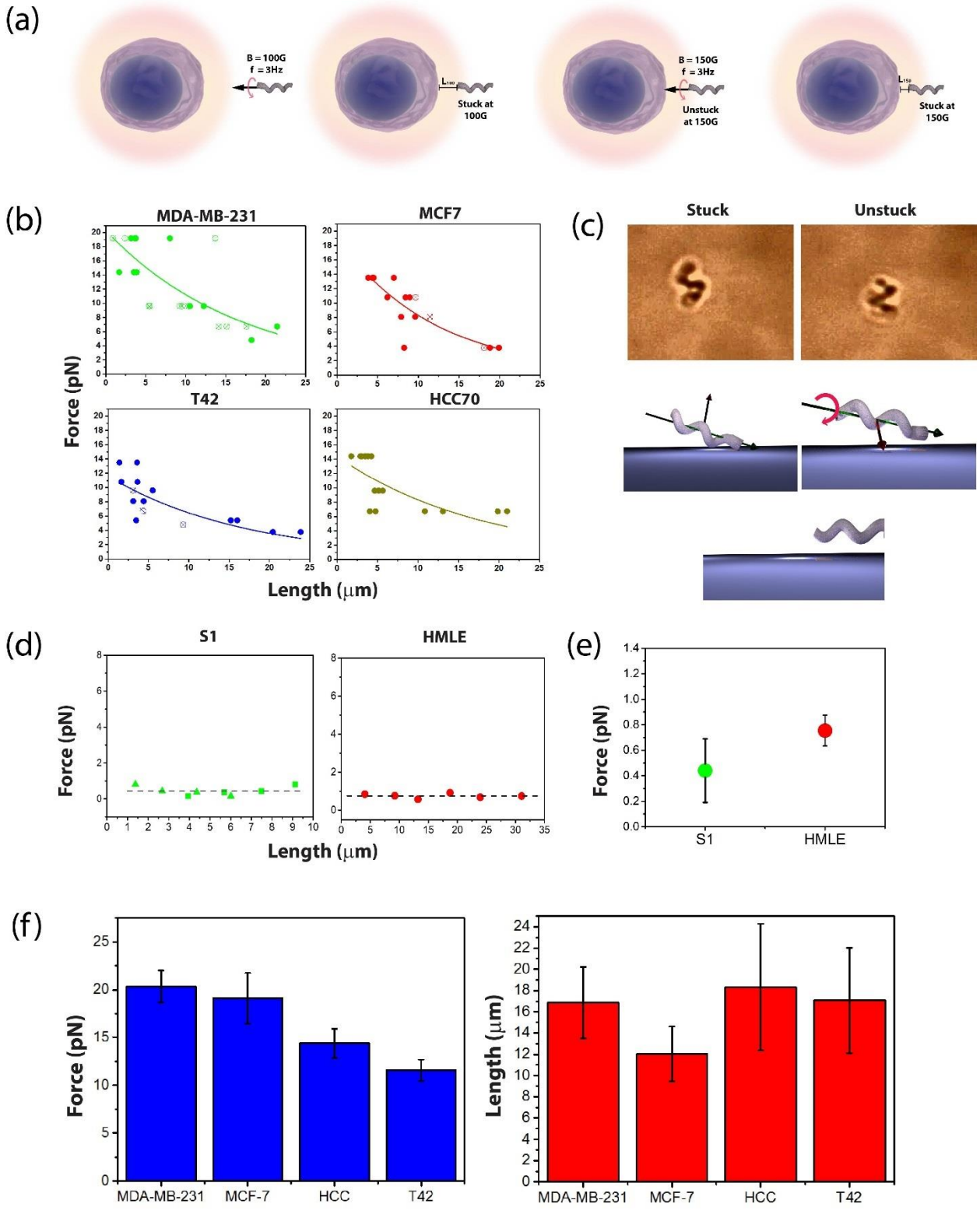

Figure 3: Adhesion force magnitude and distance dependence for various cell lines

(a) Schematic depiction of the experimental procedure to measure the spatial dependence of the force of nanorobot-ECM adhesion. (b) Plot of average force (F) vs adhesion distance (x) for four breast cancer cells is shown. Within

each graph, open circles correspond to a single nanorobot, highlighting the self-referenced method of measurements. (c) The two frames show how a nanorobot detaches from the ECM to which it is adhered. The nanorobot rotates about its long axis under the influence of a strong magnetic force. A schematic of the detachment process is shown in the cartoon panel below. (d) Plot of average force (F) vs adhesion distance (x) generated by a nanorobot from the drag it overcomes while swimming near two non-transformed breast cells is shown. (e) Graph depicting drag force (Mean ± SD) overcome by nanorobots while swimming near non-transformed breast cells. (f) The fitting formula $F = F_0 \exp\left(\frac{-x}{l_p}\right)$ provides characteristics force (F_0) and length (l_p) scales, as described in the main text. Estimated F_0 (left) and l_p (right) for various cell line shown as bar graphs (Mean ± SD).

The strength of magnetic field required to overcome adhesion of nanorobots to ECM depends on cellular context

Next, we quantified the adhesive force of nanorobots near cancer cells. The procedure is shown schematically in Figure 3(a). We directly imaged the nanorobot as it was driven through rBM towards a viable cancer cell till it got adhered to the adjacent ECM. At this time, the distance of the nanorobot from the nearest cell membrane was measured (see movie M2a). The field at which the nanorobot got adhered to the ECM could be related to the maximum available torque ($\tau = m \times B = \frac{\Omega_1 \eta f_g}{\sin(\theta_m)}$) , which in turn estimates the effective force of adhesion, given by $F = \frac{2\tau}{t} = \frac{2\Omega_1 \eta f_g}{t\, sin(\theta_m)}$. In the expression of force F, m is the magnetic moment of the nanorobot and t is the thickness, here the filament diameter of the helix (see SI: Figure S1(a)), $\Omega_1$is a characteristic cutoff frequency (see SI: Section S5), η is the viscosity of the fluid, $f_g$is a geometrical factor related to the drag coefficient of a rod rotating about the short axis and θ_m is angle between the direction of magnetization and the short axis. The strength of applied field lies in the range between 50 and 250 Gauss. The method to estimate m has been described in previous papers[37,53] and also discussed in the supporting information (see SI: Section S5 and Figure S5). The adhesive force, thus calculated, gives an estimate of the rotational force exerted by the nanorobot that is just enough to

drive it to the point in the ECM where it gets adhered. A higher field would be necessary to overcome the adhesion and move further near the cell membrane. To quantify the adhesion data in more general terms, we fit an exponential function of the form: $F = F_0 \exp\left(\frac{-x}{l_p}\right)$, where x is the distance of the nanorobot from the cell surface. The fitting has two parameters which represent a characteristic force (F_0) and a characteristic length (l_p) scale for different cell lines. The variation of F as a function of distance, along with the best fit curve is shown in Figure 3(b).

For a few nanorobots, it was indeed possible to get the robot detached from the ECM by just increasing the field strength by another 50 or 100 Gauss. The relation between applied torque and adhesive force described earlier could be understood from the way the nanorobot detached from the ECM, shown with schematics and microscopic images in Figure 3(c). The corresponding measurements are intrinsically self-referenced in nature, since the same robot shows attachment to the ECM and subsequent detachment under higher field. The estimates of adhesion force for nanorobots which could be detached are represented by the open circles in Figure 3(b). However, detachment from ECM was not always possible, as the highest field strength available from our setup (250 Gauss) was not always enough to generate the torque needed to move an adhered nanorobot.

We used four different breast cancer cell lines with variable extents of invasiveness and metastatic ability: MDA-MB-231, a triple negative cancer cell line that shows an invasive ‘stellate’-like growth phenotype, when cultured on rBM matrix; MCF7, HCC70 and T42 represent three breast cancer cell lines that show a milder ‘mass’-like morphologies on rBM matrices[54,55] (See SI: Table S1 for a description of the cell lines used in this study). Control experiments with untransformed breast epithelial cells HMLE and S1, the latter being an isogenic non-transformed counterpart of the malignant T42 mentioned above[56] did not show any adhesion for field strengths of 50 Gauss

(see movie M2b and M2c). The maximum force of adhesion provided by the non-transformed cells, where adhesion was not observed, was estimated by calculating the drag overcome by the nanorobot while swimming in the matrix (see Figure 3(d) and (e)). Approximating the shape of nanorobots as ellipsoids, the force F is represented as[57]: $F = \frac{4\eta\pi aV}{[\ln\left(\frac{2a}{b}\right)-\frac{1}{2}]}$, where a and b are the dimensions of the semi-major and semi-minor axes respectively, η the viscosity of the surrounding medium, and V is the speed of the nanorobot.

As shown in Figure 3(f), the characteristic length l_p does not vary significantly for four different cell lines viz. MDA-MB-231, MCF7, HCC70 and T42. However, there is significant difference in the characteristic force (F_0), which increases for cells with higher metastatic potential. This suggests that local remodeling of the ECM by cancer cells results in adhesion, which extends to the same length scale for all cell lines irrespective of their metastatic potential. On the other hand, the intensity of the source of adhesion varies for different cell lines and shows an association with their metastatic potential.

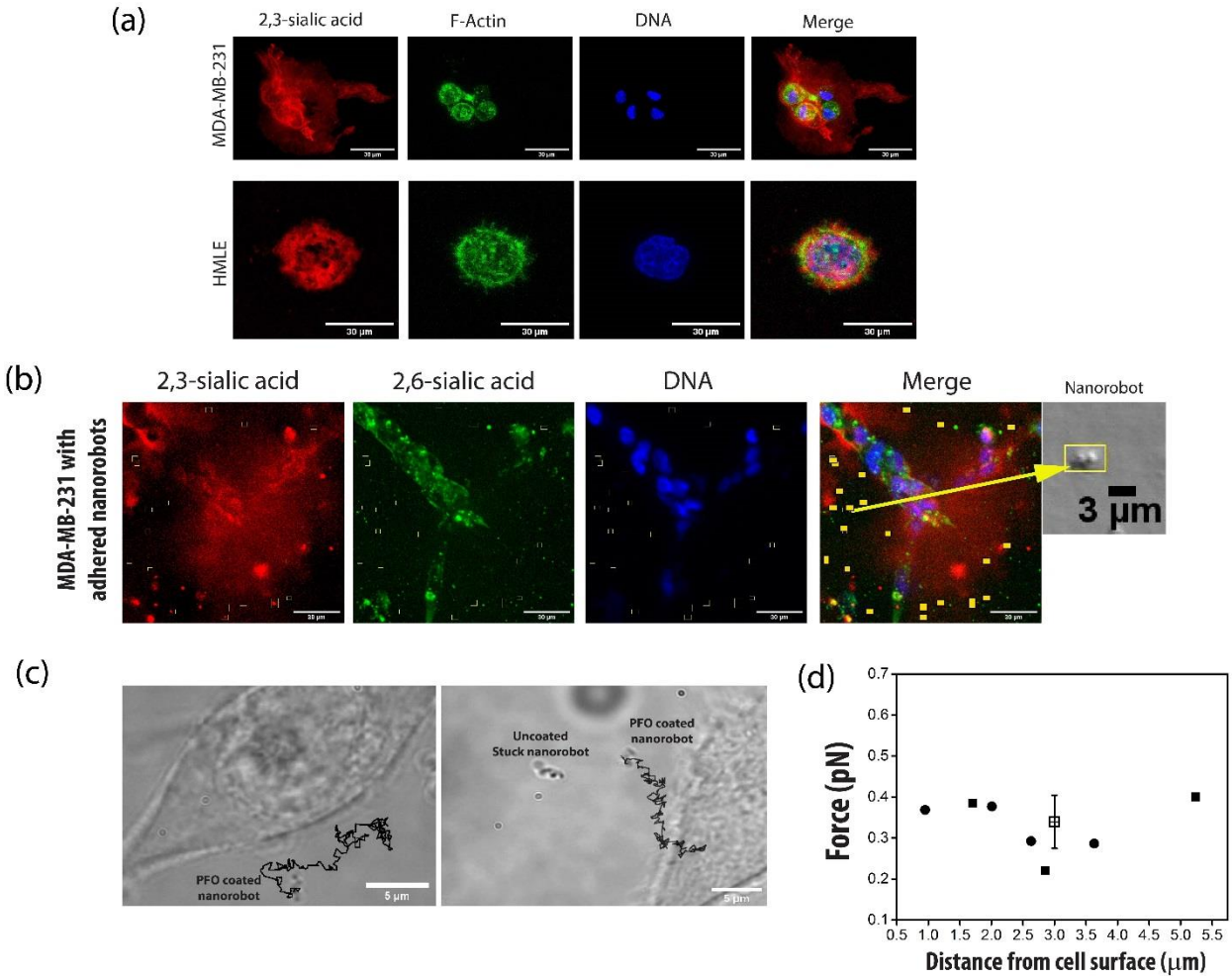

Figure 4: Role of sialylation in the preferential adhesion of the nanorobots near CC

(a) Representative image showing the distinct presence of α2,3-linked sialic acid (red) in the ECM surrounding MDA-MB-231(CC) cell. The F-Actin (green) and DNA (blue) are stained to mark the cortical cytoplasm and nuclear material respectively (similar staining was observed in three independent biological repeats). Lower panel shows cell surface localization of α2,3-linked sialic acid in a HMLE cell (NC). (b) Representative photomicrograph of MDA-MB-231(CC) cells showing the coincidence in localization of adhered nanorobots and extracellular α2,3-linked sialic acid (red) in the ECM. (Red: α2,3-linked sialic acid using MAA-TRITC, Green: cell surface staining with α-2,6-linked sialic acid using SNA-FITC, Blue: DNA). All nanorobots in various planes have been highlighted in yellow on the maximum intensity z-projection. All scale bars denote 30 µm. (c) Effect of 1H, 2H, 2H-Perfluorooctyltriethoxysilane (PFO) coating on nanorobots. PFO-coated nanorobots do not get adhered to the CC, unlike uncoated robots which adhere to the ECM. (d) Estimate of force from drag for PFO-coated nanorobots. The box represent the mean ± SD for two experiments.

The ECM in the vicinity of cancer cells is rich in α2,3-linked sialic acid-containing glycoconjugates

The data presented so far clearly indicates the presence of an adhesive factor near cancer cells, which is absent in the ECM surrounding non-transformed cells. An alternative possibility is the steric hindrance brought about by ECM macromolecules, as well as the possibility of macromolecules adsorbed on the robot surface to reduce the effective helicity of the structure[50]. In both these cases, the dynamics would resemble that of a rotating cylinder, implying rotation with zero net translation. This was clearly not observed in our case, and therefore we hypothesized that the swimmers adhere in a charge-dependent mechanism to the surrounding matrix. The cancer matrisome is mostly comprised of glycoproteins and proteoglycans, which may have variable extents of sialylation. Sialic acids impart negative charge to their conjugates and are known to regulate steps of carcinogenesis and cancer dissemination[58] . We used lectin fluorescent cytochemistry to assay for the spatial localization of sialic acids. TRITC-conjugated MAA (*Maackia Amurensis* Agglutinin) was used to detect α2,3-linked sialic acids (red) whereas Phalloidin-Alexa 488 was used to visualize cortical F-actin which is present at the cytoplasmic boundary as shown in Figure 4(a). It was observed that the spatial extent of α2,3-linked sialic acid staining in the ECM was congruent with the length scale (about 40 μm from the cell surface) at which nanorobots are shown to encounter prominent adhesion around cancer cells (see Figure 4(b)). This spread of sialic acid linkage localization was not observed in the ECM proximal to non-transformed cells, suggesting that cancer epithelia-secreted negatively charged α2,3-linked sialoconjugated ECM may be the primary cause of adhesion. The similarity in length scales of nanorobot adhesion between different cell lines suggests an interesting possibility: expression of matrix proteins, which are putative candidates for α2,3-linked sialoconjugation may be expressed

to the same spatial extent by different cell lines; however, more aggressive the cell line, the greater the sialylation of the conjugate(s).

To confirm the charge-based mechanism of adhesion in the vicinity of cancer cells, we tried an alternate surface functionalization on the nanorobots. The nanorobot surface was coated with 1H, 1H, 2H, 2H-Perfluorooctyltriethoxysilane (PFO) to make the surface non-adhesive to the charged ECM and such nanorobots were driven using a 100 Gauss field at 3Hz frequency. The surface-coating of silica nanorobots with PFO was confirmed by FTIR (see SI: Figure S6). It was observed that adhesion of nanorobots to ECM in the vicinity of the cancer cells was substantially reduced and there were instances of a nanorobot probing the cell surface for longer periods of time, without adhesion as evident from the trajectory plot in Figure 4(c) (also see movie M4). However, in the control experiment with uncoated nanorobots, adhesion was still observed. Even with a higher field of 150 to 200 Gauss, it was not possible to dislodge the nanorobots that were adhered to ECM. Experiments, where nanorobots coated with PFO and uncoated nanorobots were simultaneously driven towards the cancer cells preferential adhesion of uncoated nanorobots to the ECM was clearly seen (see Figure 4(c) right panel and movie M5). An estimate of force based on the drag for PFO-coated nanorobots is shown in Figure 4(d).

The spatial extent (~ 40 μm) of the remodeling induced by cancer cells was also observed in scanning electron microscope images. As shown in SI: Figure S7, the topographical properties of the surface of fixed samples show clear evidence of modified ECM in the CC microenvironment, whereas no such change was observed for the NC microenvironment. The topography of cancer-secreted ECM could also be contrasted with the scanning electron microscope image of rBM at the concentration used for all our experiments as shown in SI: Figure S8. rBM under scanning

electron microscope appears dense and sterically constrained when compared to the remodeled matrix in the vicinity of cancer cells.

(a) Sialic Acid Distribution in MCF-7

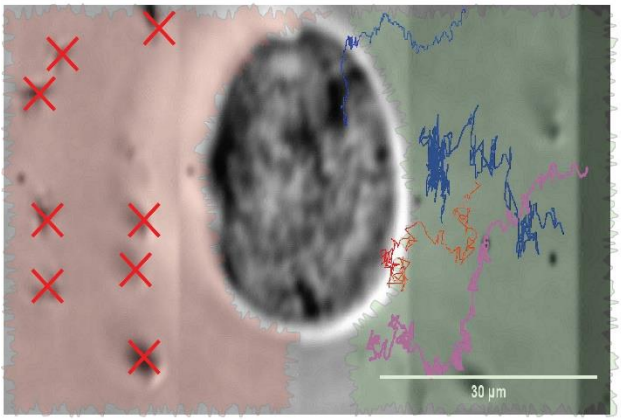

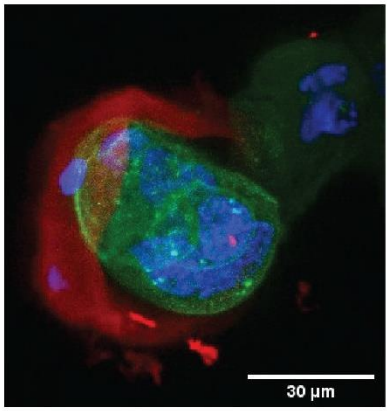

(b) Sialic Acid Distribution in MDA-MB-231

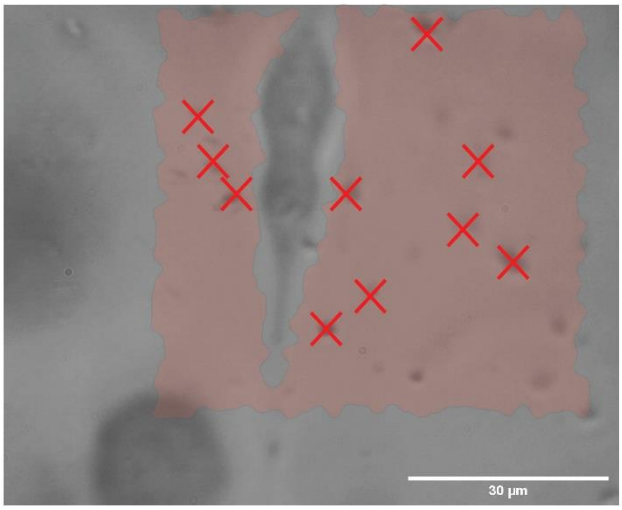

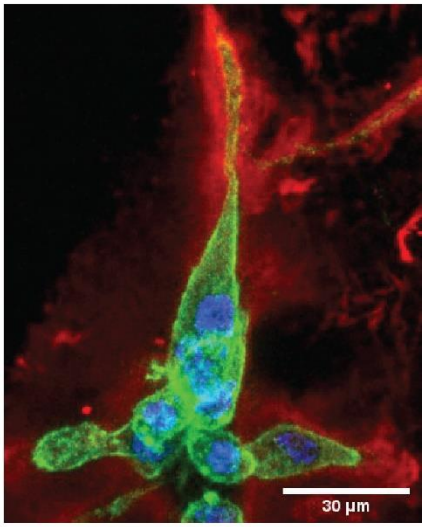

(c)

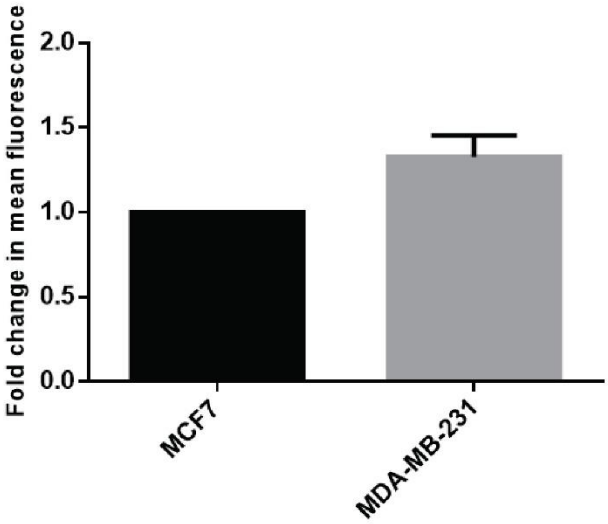

Figure 5: Anisotropy of nanorobot adhesion to MCF7 milieu is correlated with anisotropy in ECM sialylation

(a) Representative image of MCF7 observed under a brightfield microscope with nanorobots propelling towards the cell. The left region of the cell shaded in red has many nanorobots adhered to the ECM which are not responsive to the applied magnetic field. The nanorobots not responding to the applied magnetic field are denoted by red cross symbols. The trajectories of nanorobots approaching from the right are plotted in the region shaded green. No adhesion is observed here. The fluorescence image in the right panel confirms the anisotropic distribution of sialylated ECM in MCF7 cells. (b) Representative brightfield image of MDA-MB-231 cell with nanorobots adhered all around it. Fluorescence image confirms a rather isotropic distribution of sialylated ECM. Non-responsive nanorobots are denoted by red cross symbols. (c) Quantification of sialic acid signal levels present in ECM around MCF7 and MDA-MB-231 cells. The bar graph represents fold change in α2,3-linked sialic acid levels measured through fluorescence intensity of conjugated TRITC (mean ± SD; 3 independent experiments). The comparison was done with ratio-paired t-test. ($p = 0.04$)

Isotropy in spatial distribution of α2,3-sialylated ECM and nanorobot adhesion is specific to cancer cell type

While driving the nanorobots towards various cell lines, it was often observed that the adhesion was anisotropic for MCF7 cells: the nanorobots could approach the cells from one direction with minimum adhesion, but substantial adhesion was observed when nanorobots were driven from another direction. However, such angle dependence was not observed for MDA-MB-231 cells. As shown in the fluorescent image in Figure 5(a), the MCF7 cells secrete sialylated ECM in an asymmetric fashion. The pattern of adhesion of the nanorobots in the vicinity of such cells was also recorded. Nanorobots actuated in rBM seeded with MCF7 cells were subjected to a magnetic field of 50 Gauss rotating at a frequency of 3Hz and allowed to approach MCF7 cells. The cells and nanorobots were observed at different spatial locations throughout the duration of the experiment which lasted about an hour. It was observed that nanorobots often adhere preferentially along one particular direction relative to MCF7. Some nanorobots were observed to approach MCF7 from one side and reach the cell membrane, where they adhered to the membrane. However, all nanorobots on opposite side of the cell were found to be adhered at some distance as seen in Figure 5(a). On the other hand, nanorobots adhered uniformly around MDA-MB-231 cells within

length scale of 40 μm which corroborates with our earlier experiments. Such anisotropy can be corroborated with the sialic acid distribution in the ECM surrounding the cells.

The MDA-MB-231 cells have a secretion pattern that is isotropic around the cell surface (see Figure 5(b)). This observation reinforces the spatial association between the distribution of sialylated ECM in the vicinity of cancer cells and the distribution of nanorobot-ECM adhesion. Further, the staining intensity of α2,3-linked sialic acids in the ECM surrounding MCF7 was lower than that for MDA-MB-231 cells (see Figure 5(c)) suggesting a direct correlation between the characteristic force required to move nanorobots and the sialylation of the matrix through which they are being moved (see characteristic force F_0, for MCF7 and MDA-MB-231 in Figure 3(c)).

Conclusions

We demonstrated how the dynamics of nanorobot maneuverability can be used to spatially differentiate between cancerous and non-cancerous cell niches that were engineered to coexist within a tissue-like microenvironment. Our observations were consistent across four distinct breast cancer cell lines (and 2 non-cancerous breast epithelial lines), which suggests this observation may be applicable across malignant neoplasms of other organs. We find that the physical effects of invading cancer cells are manifest up to a length of ~40 μm from the cell surface within the ECM surrounding them. The adhesive force measurements provide a direct insight into how the presence of charged sialic acids within ECM secreted by cancer cells can be correlated to their metastatic potential. Hypersialylation of tumor cells has for long been demonstrated in multiple cancers[59–62]; however, these studies pertain to the effects on cancer cell behavior by sialic acids that are conjugated to glycoproteins localized on cell surfaces. In this manuscript, we observe specific sialic acid linkages within the ECM secreted by the cells. The proteins that are secreted by cancer cells and constitute their surrounding ECM are collectively referred to as the cancer matrisome[2,63],

which has been demonstrated to be chemically distinct from that of normal cells[64]. Here as we show for the first time, the cancer matrisome not only shows distinct signatures of glycosylation, the latter renders its mechanochemical properties distinct from that of untransformed cells.

Cancer cells have been shown to remodel their surrounding matrix microenvironments through multiple mechanisms: through secretion of metalloproteinases that degrade matrix proteins [65], expression of lysyl oxidases that crosslink collagen fibers [66], and synthesis of proteoglycans that can modulate the fibrillar topography [67]. We believe that our observed length scale of ~40 µm may represent the spatial transition between the synthetic (proximal to the cancer cells) and degradative (distal) remodeling processes. Therefore, our findings suggest a simple and yet elegant method of targeting cancer cell niche with enough specificity. We believe these findings will find use as targeting strategies in future in-vivo applications, in quantification of cancer aggression and as biophysical probes to study the extracellular environment of cancer.

Materials and methods

Fabrication of thin nanorobots: To fabricate thin nanorobots it was necessary to reduce the seed layer size while maintaining enough distance between subsequent seeds to allow shadowing during evaporation. This was achieved by using Langmuir Blodgett layers of 700 nm polystyrene beads. After monolayer formation, the beads were etched down to 500 nm by air plasma etching. The etched sample was further subjected to reactive ion etching to create 1 µm pillars on the silicon wafer (see SI: Figure S2(d)). The top of the 1 µm pillars was coated with a thin film of 18 nm silver which was subsequently annealed at 300^0 C for 15 minutes to form silver balls of diameter 200 nm. This was used as the seed layer for Glancing Angle Deposition (GLAD) of silica in which the magnetic material made of iron and cobalt powder mixed in 1:1 (w/w) ratio was integrated

inline during the shadow growth. This ensured encapsulation of the magnetic material by silica, thus shielding it from the external environment and preventing etching and degradation under extreme conditions.

Statistics:

Data was analyzed using Origin 9.1, MATLAB 2015b and ImageJ. All data are presented as means ± standard deviations (SDs). Comparison of counts between distinct groups was made by t-test of proportions.

Cell culture:

HMLE cells were a kind gift from Prof. Robert Weinberg, Harvard Medical School and Dr. Annapoorni Rangarajan, Indian Institute of Science. These cells were cultured in DMEM:F12 (1:1) (HiMedia, AT140) supplemented with 1% fetal bovine serum (Gibco, 10270), 0.5 µg/mL Hydrocortisone (Sigma, H0888), 10 µg/mL Insulin (Sigma, I6634) and 10 ng/mL human recombinant epidermal growth factor (HiMedia, TC228). MDA-MB-231 and HCC70 cells were grown in DMEM:F12 (1:1) along with 10% fetal bovine serum. MCF7 cells were maintained in DMEM (HiMedia, AT007F) supplemented with 10% fetal bovine serum. S1 and T42 cells were cultures as described elsewhere[68]. All the cells were maintained in a humidified chamber at 37^0 C temperature and 5% carbon dioxide.

3D culture and experimental procedure:

In case of single cell line 3D culture, 5×10^4 cells were mixed in 50 µl of rBM (Corning, 354230) and allowed to solidify at 37^0 C temperature and 5% carbon dioxide in a humidified chamber. The concentration of rBM was ~9mg/ml. For co-culture, 2.5×10^4 of HMLE and MDA-MB-231 cells were mixed in 50 µl of rBM and allowed to solidify. Cultures were grown in a defined medium[68]

for 72 hour before injecting the nanorobots. An area of 0.5 mm^2 of a wafer containing nanorobots was sonicated into a microcentrifuge tube containing 50 μl deionized water. A 10 μl solution containing 10^5 nanorobots suspended in deionized water was injected into the 3D matrix using a 26 gauge syringe. The sample was placed in a triaxial Helmholtz coil mounted on an optical microscope (Olympus IX71) and imaged through a 50x (or 100x) objective lens. The nanorobots were observed while the field was on and recorded using a CMOS camera. It was observed that at the site of injection of nanorobots many of them got adhered to the glass slide. The presence of local pockets of injected fluids has been reported in a previous literature[69], where it was shown that within a time scale of approximately 30 minutes, the system gains its structural uniformity. To be completely sure that the experiments are carried out in native rBM-cell environment, we drive the nanorobots for 30 minutes; which is at least 1000 μm away from the site of injection. We observed 0-5 nanorobots per cell at the region of experiment.

For confocal imaging, the nanorobots were actuated under 100 Gauss field rotating with a frequency of 3Hz for 30 minutes. The sample was subsequently fixed using sucrose solution after actuation. The experiments for measuring the adhesive force was generally done using 5 different field strengths (70, 100, 150, 200 and 250 Gauss) and the actuating frequency was kept either at 3Hz or 5Hz.

Cell Viability:

5000 cells were seeded in each well of a 96 well plate. After overnight culture, cells were treated with 10^5 nanorobots for 24 hours to check if they have any effect on cell viability. After 24 hours, 100 μg/mL resazurin was added to each well and incubated for 2 hours. Fluorescence was

measured at Ex 560 nm/ Em 590 nm as a read out for viability of cells. Fluorescence readings from treated cells was normalized to untreated cells.

α2,3-linked sialic acid staining:

3×10^4 cells (HMLE, MCF7 and MDA-MB-231) were seeded on top of solidified rBM in a 8-well chambered cover glass (Eppendorf, 0030742036). Cells were grown for 72 hours in defined medium[68]. Cells were washed with PBS and treated with 18% and 30% sucrose in Phosphate-Buffered Saline (PBS) respectively for 30 minuntes each at room temperature. Cells were fixed with 4% formaldehyde (Merck,1.94989.0521) for 20 minutes at room temperature and washed with PBS twice. Cells were stained with TRITC conjugated *Maackia amurensis* Lectin (MAA/MAL I) (1:200) (bioWORLD, 21510007-1) overnight at 4^0 C. After MAA staining, cells were washed with PBS thrice, 5 minutes each at room temperature and counter stained with 4,6-diamidino-2-phenylindole (DAPI) (Invitrogen, D1306) and Alexa Flour 488-conjugated Phalloidin (Invitrogen, A12379).

Laser scanning confocal microscopy:

All the images were captured using either Zeiss LSM 880 or Leica TCS SP8 confocal microscope with system optimized Z intervals. At least three random fields were imaged in each experiment. Images were processed/analysed using either Zen lite or Fiji software[70].

Quantification of α2,3-linked sialic acid in ECM:

After acquiring images, fluorescent signals from TRITC-conjugated MAA were quantified using Fiji software. Five stacks above and below from mid stack were considered for analysis. Using magic wand tool, sialic acid present in ECM and on cells was selected and integrated density of signal was recorded. Using F-actin staining, cytoplasmic boundary was determined and using magic wand tool, boundary was marked and corresponding MAA signal was recorded.

Subsequently, sialic acid signal from cells was subtracted from signal obtained from both cell and matrix. Sum of all ten stacks was represented as sialic acid present in ECM.

Estimation of the magnetic moment: The standard method of calculating the magnetic moment of a nanorobot has been described in previous literature in great details (also see SI: Section S5 and Figure S5(c)). A microfluidic chamber was made using a coverslip on a glass slide, in which nanorobot solution was placed. The chamber was placed under the microscope in a Helmholtz coil and subjected to 30 Gauss field while the frequency was varied from 1Hz to 10Hz. The precession angle of the nanorobot was recorded and a frequency vs precession angle curve was plotted. The frequency where the nanorobot changed its precession angle from 90^0 (tumbling state) to a lower angle (precession state) was calculated by proper fit. This was done at regular intervals over the time period when the experiments were conducted. Initial magnetic moment was calculated to be $\sim 1.01 \times 10^{-16} Am^2$. However, since the same sample was used for all our experiments involving force calculations, the magnetic moment was found to have weakened to a value of $5 \times 10^{-17} Am^2$ after a period of 12 months.

Coating of PFO on nanorobots: To coat nanorobots with PFO the wafer containing nanorobots was placed in vacuum with about 20 µl of PFO and left overnight. This was enough to coat nanorobots with PFO as seen from the FTIR data (SI: Figure S6).

References:

1. Friedl, P. & Alexander, S. Cancer Invasion and the Microenvironment: Plasticity and Reciprocity. *Cell* **147**, 992–1009 (2011).
2. Naba, A. *et al.* The extracellular matrix: Tools and insights for the “omics” era. *Matrix Biol.* **49**, 10–24 (2016).

3. Bhat, R. & Bissell, M. J. Of plasticity and specificity: dialectics of the microenvironment and macroenvironment and the organ phenotype. *Wiley Interdiscip. Rev. Dev. Biol.* **3**, 147–163 (2014).

4. Huang, S. & Ingber, D. E. Cell tension, matrix mechanics, and cancer development. *Cancer Cell* **8**, 175–176 (2005).

5. Cao, Y., DePinho, R. A., Ernst, M. & Vousden, K. Cancer research: past, present and future. *Nat. Rev. Cancer* **11**, 749–754 (2011).

6. Shamir, E. R. & Ewald, A. J. Three-dimensional organotypic culture: experimental models of mammalian biology and disease. *Nat. Rev. Mol. Cell Biol.* **15**, 647–664 (2014).

7. Hoarau-Véchot, J., Rafii, A., Touboul, C. & Pasquier, J. Halfway between 2D and Animal Models: Are 3D Cultures the Ideal Tool to Study Cancer-Microenvironment Interactions? *Int. J. Mol. Sci.* **19**, 181 (2018).

8. Nelson, C. M. & Bissell, M. J. Modeling dynamic reciprocity: Engineering three-dimensional culture models of breast architecture, function, and neoplastic transformation. *Semin. Cancer Biol.* **15**, 342–352 (2005).

9. Langhans, S. A. Three-Dimensional in Vitro Cell Culture Models in Drug Discovery and Drug Repositioning. *Front. Pharmacol.* **9**, 6 (2018).

10. Riedl, A. *et al.* Comparison of cancer cells in 2D vs 3D culture reveals differences in AKT-mTOR-S6K signaling and drug responses. *J. Cell Sci.* **130**, 203–218 (2017).

11. Li, W.-J., Laurencin, C. T., Caterson, E. J., Tuan, R. S. & Ko, F. K. Electrospun nanofibrous structure: A novel scaffold for tissue engineering. *J. Biomed. Mater. Res.* **60**, 613–621 (2002).

12. Chhetri, R. K. *et al.* Probing biological nanotopology via diffusion of weakly constrained

plasmonic nanorods with optical coherence tomography. *Proc. Natl. Acad. Sci. U. S. A.* **111**, E4289-97 (2014).

13. Blackmon, R. L. *et al.* Imaging Extracellular Matrix Remodeling In Vitro by Diffusion-Sensitive Optical Coherence Tomography. *Biophysj* **110**, 1858–1868 (2016).
14. Raeesi, V., Chan, W. C. W. & Chan, W. C. W. Improving Nanoparticle Diffusion in a Tumor Collagen Matrix by Photo-thermal Gold Nanorods Improving nanoparticles diffusion inside tumor collagen by photo-thermal gold nanorods. *Nanoscale* **8**, 12524–12530 (2016).
15. Schenke-Layland, K. Non-invasive multiphoton imaging of extracellular matrix structures. *J. Biophotonics* **1**, 451–462 (2008).
16. Alcaraz, J., Otero, J., Jorba, I. & Navajas, D. Bidirectional mechanobiology between cells and their local extracellular matrix probed by atomic force microscopy. *Semin. Cell Dev. Biol.* **73**, 71–81 (2018).
17. Jorba, I., Uriarte, J. J., Campillo, N., Farré, R. & Navajas, D. Probing Micromechanical Properties of the Extracellular Matrix of Soft Tissues by Atomic Force Microscopy. *J. Cell. Physiol.* **232**, 19–26 (2017).
18. Jones, D. P., Hanna, W. & Celli, J. P. Mapping dynamic mechanical remodeling in 3D tumor models via particle tracking microrheology. **9327**, 93270L (2015).
19. Wirtz, D. Particle-Tracking Microrheology of Living Cells: Principles and Applications. *Annu. Rev. Biophys.* **38**, 301–326 (2009).
20. Rowe, R. G. & Weiss, S. J. Breaching the basement membrane: who, when and how? *Trends in Cell Biology* **18**, 560–574 (2008).
21. Ormerod, E. J., Warburton, M. J., Hughes, C. & Rudland, P. S. Synthesis of basement

membrane proteins by rat mammary epithelial cells. *Dev. Biol.* **96**, 269–275 (1983).

22. Albrechtsen, R., Nielsen, M., Wewer, U., Engvall, E. & Ruoslahti, E. Basement membrane changes in breast cancer detected by immunohistochemical staining for laminin. *Cancer Res.* **41**, 5076–81 (1981).
23. Abdelkarim, M. *et al.* Invading Basement Membrane Matrix Is Sufficient for MDA-MB-231 Breast Cancer Cells to Develop a Stable In Vivo Metastatic Phenotype. *PLoS One* **6**, e23334 (2011).
24. Kenny, P. A. *et al.* The morphologies of breast cancer cell lines in three-dimensional assays correlate with their profiles of gene expression. *Mol. Oncol.* **1**, 84–96 (2007).
25. Bergstraesser, L. M. & Weitzman, S. A. Culture of normal and malignant primary human mammary epithelial cells in a physiological manner simulates in vivo growth patterns and allows discrimination of cell type. *Cancer Res.* **53**, 2644–54 (1993).
26. Ghosh, A. & Fischer, P. Controlled propulsion of artificial magnetic nanostructured propellers. *Nano Lett.* **9**, 2243–2245 (2009).
27. Zhang, L. *et al.* Artificial bacterial flagella: Fabrication and magnetic control. *Appl. Phys. Lett.* **94**, 064107 (2009).
28. Fischer, P. & Ghosh, A. Magnetically actuated propulsion at low Reynolds numbers: towards nanoscale control. *Nanoscale* **3**, 557–563 (2011).
29. Mandal, P., Patil, G., Kakoty, H. & Ghosh, A. Magnetic Active Matter Based on Helical Propulsion. *Acc. Chem. Res.* **51**, 2689–2698 (2018).
30. Abbott, J. J. *et al.* How Should Microrobots Swim? *Int. J. Rob. Res.* **28**, 1434–1447 (2009).
31. Peters, C., Hoop, M., Pané, S., Nelson, B. J. & Hierold, C. Degradable Magnetic

Composites for Minimally Invasive Interventions: Device Fabrication, Targeted Drug Delivery, and Cytotoxicity Tests. *Adv. Mater.* **28**, 533–538 (2016).

32. Kim, S. *et al.* Fabrication and Characterization of Magnetic Microrobots for Three-Dimensional Cell Culture and Targeted Transportation. *Adv. Mater.* **25**, 5863–5868 (2013).

33. Venugopalan, P. L., Jain, S., Shivashankar, S. & Ghosh, A. Single coating of zinc ferrite renders magnetic nanomotors therapeutic and stable against agglomeration. *Nanoscale* **10**, 2327–2332 (2018).

34. Venugopalan, P. L. *et al.* Conformal Cytocompatible Ferrite Coatings Facilitate the Realization of a Nanovoyager in Human Blood. *Nano Lett.* **14**, 1968–1975 (2014).

35. Wu, Z. *et al.* A swarm of slippery micropropellers penetrates the vitreous body of the eye. *Sci. Adv.* **4**, eaat4388 (2018).

36. Pal, M. *et al.* Maneuverability of Magnetic Nanomotors Inside Living Cells. *Adv. Mater.* **30**, 1800429 (2018).

37. Ghosh, A. A. *et al.* Helical Nanomachines as Mobile Viscometers. *Adv. Funct. Mater.* **28**, 1705687 (2018).

38. Ghosh, S. & Ghosh, A. Mobile nanotweezers for active colloidal manipulation. *Sci. Robot.* **3**, eaaq0076 (2018).

39. Mandal, P., Chopra, V. & Ghosh, A. Independent Positioning of Magnetic Nanomotors. *ACS Nano* **9**, 4717–4725 (2015).

40. Schamel, D. *et al.* Nanopropellers and Their Actuation in Complex Viscoelastic Media. *ACS Nano* **8**, 8794–8801 (2014).

41. Li, J., Esteban-Fernández De Ávila, B., Gao, W., Zhang, L. & Wang, J. Micro/nanorobots

for biomedicine: Delivery, surgery, sensing, and detoxification. *Sci. Robot* **2**, (2017).

42. Gao, W., de Ávila, B. E. F., Zhang, L. & Wang, J. Targeting and isolation of cancer cells using micro/nanomotors. *Advanced Drug Delivery Reviews* **125**, 94–101 (2018).
43. Balasubramanian, S. *et al.* Micromachine-Enabled Capture and Isolation of Cancer Cells in Complex Media. *Angew. Chemie Int. Ed.* **50**, 4161–4164 (2011).
44. Gao, W. *et al.* Artificial Micromotors in the Mouse's Stomach: A Step toward in Vivo Use of Synthetic Motors. *ACS Nano* **9**, 117–123 (2015).
45. Ullrich, F. *et al.* Swimming Characteristics of Helical Microrobots in Fibrous Environments. *2016 6th IEEE Int. Conf. Biomed. Robot. Biomechatronics* 1–6 (2015). doi:10.1109/BIOROB.2016.7523671
46. Conklin, M. W. *et al.* Aligned Collagen Is a Prognostic Signature for Survival in Human Breast Carcinoma. *Am. J. Pathol.* **178**, 1221–1232 (2011).
47. Tomasetti, L. & Breunig, M. Preventing Obstructions of Nanosized Drug Delivery Systems by the Extracellular Matrix. *Adv. Healthc. Mater.* **7**, 1700739 (2018).
48. Dancy, J. G. *et al.* Non-specific binding and steric hindrance thresholds for penetration of particulate drug carriers within tumor tissue. *J. Control. Release* **238**, 139–148 (2016).
49. Anguiano, M. *et al.* Characterization of three-dimensional cancer cell migration in mixed collagen-Matrigel scaffolds using microfluidics and image analysis. *PLoS One* **12**, e0171417 (2017).
50. Walker, D., Kasdorf, B. T., Jeong, H.-H., Lieleg, O. & Fischer, P. Enzymatically active biomimetic micropropellers for the penetration of mucin gels. *Sci. Adv.* **1**, e1500501 (2015).
51. Eble, J. A. & Niland, S. The extracellular matrix in tumor progression and metastasis.

Clinical and Experimental Metastasis **36**, 171–198 (2019).

52. Walker, C., Mojares, E. & del Río Hernández, A. Role of Extracellular Matrix in Development and Cancer Progression. *Int. J. Mol. Sci.* **19**, 3028 (2018).

53. Ghosh, A., Mandal, P., Karmakar, S. & Ghosh, A. Analytical theory and stability analysis of an elongated nanoscale object under external torque. *Phys. Chem. Chem. Phys.* **15**, 10817–23 (2013).

54. Lee, G. Y., Kenny, P. A., Lee, E. H. & Bissell, M. J. Three-dimensional culture models of normal and malignant breast epithelial cells. *Nat. Methods* **4**, 359–365 (2007).

55. Pally, D., Pramanik, D. & Bhat, R. An Interplay Between Reaction-Diffusion and Cell-Matrix Adhesion Regulates Multiscale Invasion in Early Breast Carcinomatosis. *Front. Physiol.* **10**, 790 (2019).

56. Weaver, V. M., Howlett, A. R., Langton-Webster, B., Petersen, O. W. & Bissell, M. J. The development of a functionally relevant cell culture model of progressive human breast cancer. *Semin. Cancer Biol.* **6**, 175–184 (1995).

57. Berg, H. C. *Random walks in biology*. (Princeton University Press, 1993).

58. Vajaria, B. N. & Patel, P. S. Glycosylation: a hallmark of cancer? *Glycoconj. J.* **34**, 147–156 (2017).

59. Bhat, R. *et al.* Nuclear repartitioning of galectin-1 by an extracellular glycan switch regulates mammary morphogenesis. *Proc. Natl. Acad. Sci.* **113**, E4820–E4827 (2016).

60. Bull, C., Stoel, M. A., den Brok, M. H. & Adema, G. J. Sialic Acids Sweeten a Tumor's Life. *Cancer Res.* **74**, 3199–3204 (2014).

61. Pearce, O. M. T. & Läubli, H. Sialic acids in cancer biology and immunity. *Glycobiology* **26**, 111–128 (2016).

62. Rodrigues, E., Macauley, M., Rodrigues, E. & Macauley, M. S. Hypersialylation in Cancer: Modulation of Inflammation and Therapeutic Opportunities. *Cancers (Basel).* **10**, 207 (2018).

63. Hynes, R. O. The extracellular matrix: not just pretty fibrils. *Science* **326**, 1216–9 (2009).

64. Naba, A., Clauser, K. R., Lamar, J. M., Carr, S. A. & Hynes, R. O. Extracellular matrix signatures of human mammary carcinoma identify novel metastasis promoters. *Elife* **3**, (2014).

65. Kessenbrock, K., Plaks, V. & Werb, Z. Matrix Metalloproteinases: Regulators of the Tumor Microenvironment. *Cell* **141**, 52–67 (2010).

66. Levental, K. R. *et al.* Matrix crosslinking forces tumor progression by enhancing integrin signaling. *Cell* **139**, 891–906 (2009).

67. Theocharis, A. D. *et al.* Insights into the key roles of proteoglycans in breast cancer biology and translational medicine. *Biochim. Biophys. Acta - Rev. Cancer* **1855**, 276–300 (2015).

68. Blaschke, R. J., Howlett, A. R., Desprez, P.-Y., Petersen, O. W. & Bissell, M. J. [25] Cell differentiation by extracellular matrix components. *Methods Enzymol.* **245**, 535–556 (1994).

69. Pal, M. *et al.* Helical nanobots as mechanical probes of intra- and extracellular environments. *J. Phys. Condens. Matter* (2020). doi:10.1088/1361-648X/ab6f89

70. Schindelin, J. *et al.* Fiji: an open-source platform for biological-image analysis. *Nat. Methods* **9**, 676–682 (2012).

Acknowledgement:

We thank www.somersault1824.com for providing a 'Library of Science and Medical Illustrations' under a Creative Commons license which was used for illustrating the cells in this paper. We acknowledge the nanobio group, especially Malay Pal for helpful discussions and technical support from the IISc Bioimaging facility. We thank Gouri Patil for helping with our experiments. We also acknowledge usage of the facilities available at the Centre for Nano Science and Engineering, IISc.

Funding: This research was supported in part by DBT and DST. DDG and DP like to thank IISc and the Ministry of Human Resource Development (MHRD), Government of India for providing the Senior Research Fellowship (SRF). RB would like to acknowledge support from the SERB ECR Grant (1586), Wellcome Trust-DBT India Alliance Fellowship (WELT0041), and the DBT-IISc partnership program (BT/PR27952/INF/22/212/2018).